Linking pore network characteristics extracted from CT images to the transport of solute and colloid tracers in soils under different tillage managements

*Diego Soto-Gómez[1,2], Paula Pérez-Rodríguez[1,2,3], Laura Vázquez Juíz[1,2], J. Eugenio López-Periago[1,2], and Marcos Paradelo[1,2,4]

[1]Soil Science and Agricultural Chemistry Group, Department of Plant Biology and Soil Science, Faculty of Sciences, University of Vigo, E-32004 Ourense, Spain.

[2] Hydraulics Laboratory, Campus da Auga, Facultade de Ciencias, Campus da Auga, University of Vigo.

3Laboratory of Hydrology and Geochemistry of Strasbourg (LHyGeS)

Université de Strasbourg, Strasbourg, France.

[4]Department of Agroecology, Faculty of Sciences and Technology, Aarhus University, Blichers Allé 20, P.O. Box 50, DK-8830 Tjele, Denmark

*Corresponding author Phone: +34 988 387 070; fax: +34 988 387 001, mail: disoto@uvigo.es

ABSTRACT

Understanding relations between quantitative information of soil structure from X-ray computed tomography (CT) and soil functions is a hot topic in agronomy and soil science. The influence of tillage on macroporosity (i.e., pores measured by CT > 240 μm in all directions) could be linked with their effects on solute and colloid transport properties. The tillage will also have a crucial importance in the preferential flow, i.e., a direct flow through roots and earthworm pores. Increasing knowledge on the relationships between soil tillage, structure, and transport may contribute to a deep understanding of the key factors of soil management influencing productivity and crop health.

In this work, we used CT to characterize the macropore network (>0.24 mm) of sixteen columns (100 height × 84 diameter, mm) of adjacent plots with different soil managements: conventional with shallow tillage after sowing (4 samples), conventional with no tillage after sowing (4 samples), and organic (8 samples). The soil samples were installed in columns under a dripper, and the transport behavior was examined during a breakthrough of Br and 1-μm latex microspheres, in samples near saturation trying to reach an irrigation rate of ~10 mL h^{-1} (5.1 mm h^{-1}).

Transport of Br and latex microspheres was modeled using the two-region physical non-equilibrium model (dual porosity). The preferential flow was higher under organic management, although the pore water velocities were, in general, lower. The preferential flow of Br was correlated with the total volume of CT-macropores and the local increase in the Hounsfield value (i.e. CT matrix density, CT_{Matrix}) surrounding the macropores. The denser lining, produced by the earthworms in the inner walls of the pores, was inversely correlated with the kinetic exchange coefficient between mobile and immobile zones of the dual-porosity model. The macropore roughness indicated by the CT-macropore surface area was correlated with the solute dispersion coefficient and with the solute travel time. Finally, we found that the overall CT_{Matrix} density is inversely related to the preferential flow. The importance of the work lies in the improvement of the accuracy of predictions related to soil flow transport, especially the ones that include particles traveling across the soil.

KEYWORDS: colloid transport; macroporosity; modeling; organic farming; soil structure; soil management; soil tomography.

1 Introduction

Tillage modifies the natural soil structure by changing the bulk density, the size of the aggregates, the soil penetration resistance and the water holding capacity. The objective of tillage is to eliminate weeds and mix the soil increasing temporarily the oxygenation and the soil water holding capacity [1]. However, repeated tillage activities for several years lead to less structured and easily erodible soils [2]. No-tillage and other soil conservation methods try to decrease the biopore disruption and to preserve the natural soil pore network.

The pore network has strong effects on the ability of soil to allow the movement of water downwards and the transport soluble and particulate substances. Furthermore, the water availability and flow have a great importance in the crops: in the seedling emergence, in the size and number of roots, and in plant density [3].

Conventional and conservation tillage may produce differences in the number, shape, size, and continuity of the soil pores. No-tillage and minimum tillage techniques allow the soil to develop a complex and well-connected pore network because they do not disrupt earthworm activity, root channels and cracks [4]. The macropores and cracks represent only a small percentage of the soil pores, but they have a huge influence on the transport of water, solutes and suspended colloids. These pores can be used by the water to bypass the upper layers of the soil. Moreover, colloidal particles with attached substances (facilitated transport) can travel faster through these channels, increasing the nutrient loss by leaching [5]. Particulate organic matter, labile colloidal nutrients, virus, bacteria, and protozoa have limited mobility through the soil matrix but can travel several meters in the soil by using preferential pathways (macropores) as earthworm and root pores [6].

Usually, the role of macropores in solute and colloidal transport is studied by tracer experiments in soil columns or in the field, using soluble substances or colloids [7,8], or measuring some of the macroscopic soil characteristics like the hydraulic conductivity and the air permeability [9].

However, in the last years, X-ray CT has proved to offer important information on structural parameters of the soil pore network system, such as pore topology and morphology, without altering the sample [10]. This method has been successfully used to study the effects of soil management (conventional tillage and no-tillage) on the soil pore structure, analyze the changes in the macroporosity with depth, and the pore size distributions [11]. Other works used CT images to analyze the compaction consequences and their effects on the soil atmosphere and to determine the bulk density without altering the sample [12]. CT can be used for visualization and description of the roots [13]. In this case, there are some discrepancies between this method and a destructive one: the CT underestimates the length of the roots due to the spatial resolution of the scan.

Furthermore, CT techniques have been used successfully to estimate solute transport parameters[14,15]. Solute breakthrough studies with a continuous CT monitoring showed that the most of the solute transport occurred throughout the highly continuous biogenetic pores[16]. Naveed et al. (2013)[17] found good correlations between soil air permeability and the equivalent pore diameter divided by the tortuosity (both calculated from CT images).

In this work, we hypothesized that differences in soil structure created by different soil tillage managements, inferred from the X-ray CT derived characteristics, would influence the transport of solutes and colloids.

The objectives are: (i) to characterize the structure of a soil under different tillage managements and with different degrees of earthworm activity (deducted from the signs of surface alterations observed) ; (ii) to model the transport of Br and fluorescent microspheres; and (iii) to relate transport characteristics to CT derived characteristics in order to estimate the dynamic behaviour of colloidal particles in the soil.

2 Material & Methods

2.1 Soil Sampling

Sixteen undisturbed columns (100 height × 84 diameter, mm) were collected using PVC cases in January 2013 from two adjacent experimental parcels (Centro de Desenvolvemento Agrogandeiro, Ourense, northwestern Spain, coordinates 42.099N -7.726W WGS84). Eight undisturbed soil columns were sampled from a plot under organic management (Org) with a long historical use devoted to root crops and vegetables, with the removal of the stubble. Two subzones with different earthworm activity were identified namely high (Org. A) and low (Org. B) activity (we took 4 samples of each subzone). We consider that in these two subzones the type of pores is similar whereas the difference lies in their number and shape. This was deducted in the field from the signs of surface alteration. In a conventional zone, four columns were taken from a plot devoted to spring cereal with no-till (Conv. NT) after sowing, so the roots were preserved, and other four columns from a plot that was shallow-tilled (Conv. ST) after sowing.

The columns were extracted vertically (2-12 cm depth). They were sealed immediately and refrigerated at 4° C to prevent structure alteration before CT scanning and transport experiments. Chemical properties and texture were almost identical in bulk samples adjacent to each soil column with a pH, in 1:10 soil:water ratio, of 5.9 ±0.05. Soil texture class is sandy loam according to the USDA soil classification (Table 1).

The soil columns were also saturated from the bottom in order to get the saturated water content (θ_s). After saturation, we let the columns drain for one hour (θ), to determine the range of moistures expected during the transport experiments.

2.2 Macropore characterization with CT

The CT images were acquired with a dental 3D Cone-beam i-CAT scanner (Imaging Sciences International LLC, PA, Hatfield, USA), using 120 kV, 5 mA current and a voxel size of 0.24 mm.

The raw data were processed with the free software Image-J version 1.52a [18]. Images were cropped to fit the soil enclosed into the column, and then were converted to binary using Sauvola's auto local thresholding analysis [19], to segment soil matrix and macropores (samples of this segmentation appear in Figure 1). In order to apply this method, the following settings were used: radius of 50 pixels, parameter 1 (k value) of 0.3 and parameter 2 (r value) of 128 (default value). The value of each pixel is:

$$\text{Pixel} = (\text{pixel} > \text{mean} * (1 + k + (\text{standard deviation} / r - 1))) \qquad \text{(eq. 1)}$$

The CT-macroporosity was defined as the soil volume fraction occupied by macropores larger than 0.24 mm in any dimension, it was calculated by dividing the sum of pore voxels by the number of all voxels. The number of pores, the surface area of pore walls and their volume were calculated using the Bone-J Particle Analyzer plugin in Image-J [20]. The binary images were purified by discarding the noise (using the Despeckle noise plugin), and the connectivity was also calculated with Bone-J. The skeleton of the pore network was analyzed, obtaining the number of paths and branches, slab voxels, end-point voxels (dangling ends), and the real length (L_R) and Euclidean length (L_E) of each one. With these two parameters, we calculated the tortuosity (τ) [21]

$$\tau = L_R/L_E \qquad \text{(eq. 2)}$$

Note that this tortuosity corresponds to macropores identified by image analysis. Henceforth, we will refer to this parameter as CT-tortuosity. We are going to use the average value of all the pores, and the tortuosity of the pores larger than 10 mm.

The circularity of each pore (for each slice of the stack) was calculated using the following formula

$$Circularity = 4\pi\left(\frac{Area}{Perimeter^2}\right) \qquad \text{(eq. 3)}$$

The average CT number of the matrix (CT_{Matrix}) represents the density of the matrix measured by the X-ray absorbance using the Hounsfield scale (HU). CT_{Matrix} was calculated by excluding the macropores and the stones and considering the gray shade of each voxel using the criteria of Katuwal et al. (2015) [22]. We also separated the CT_{Matrix} values of the layer of voxels corresponding to the pore walls. In this layer, the HU was used to examine the density of the pore walls.

2.3 Breakthrough experiments

Red fluorescent polystyrene latex microspheres (Magsphere Inc., Pasadena, California) were used as colloidal tracers. The particles have a diameter of 1 ± 0.11µm with a density of 1.05 g cm^{-3}. The excitation and emission wavelengths of the fluorochrome are 505-545 and 560-630 nm, respectively.

The stock suspension, which contains 4.55×10^{10} microspheres mL^{-1}, was diluted 1:200 in a solution of 0.025 M of Br^- (KBr) to obtain a suspension 2.28×10^{8} microspheres mL^{-1}. Bromide was used as an unreactive solute tracer for comparison with the colloid tracer.

The microspheres were kept in suspension during the experiment by the application of 100 ms duration ultrasound pulses at the colloid reservoir at 1 s intervals, using an ultrasonic homogenizer (Sonopuls HD 2200, Bandelin GmbH & Co. KG, Berlin, Germany).

Each soil sample was mounted in a column on a stainless steel mesh No.18 (sieve opening = 1 mm) attached to a polypropylene funnel that conducted the outflow from the bottom to an automated fraction collector. Water and microsphere suspensions were distributed dropwise at random points on the top soil surface by a robotic arm attached to the dripper. Flow boundary conditions in all breakthrough experiments were: constant flux at the upper boundary with flow rates of approximately ~10 mL h^{-1} (5.1 mm h^{-1}) (when it was possible considering the permeability of the soil) and seepage face at the bottom. Infiltration rate varied in some columns, so the flow rate was occasionally reduced to avoid surface ponding. The fall height of drops was less than 3 mm to prevent the disruption of the soil structure.

Before the breakthrough curve (BTC) experiments, flow was stabilized with deionized water DW, and when steady state flow was reached, a pulse of microspheres suspended in the KBr solution was applied (≈ 2-3 PV). Pulses were followed by washing with DW (≈ 6-10 PV). The effluent fraction volume (≈ 4-6 mL per tube) was determined by weighing, Br concentration was measured by automated colorimetry [23], and the microsphere concentration was determined by fluorescence (Jasco Fluorescence Spectrometer, Jasco FP-750). Photometric readings were calibrated with the counting of microspheres trapped in 0.45-micron filters using fluorescence microscopy and image analysis. Correlation between the two methods was linear (R > 0.997).

After the transport experiments, the columns were carefully sliced in sections ≈ 5 mm using a nylon string and a spatula. A piston jack and a precision Vernier caliper were used to extract the soil from the ring in 5 mm steps. The slices were placed in Petri dishes to identify microsphere spots under a fluorescence laboratory magnifier. Then, soil pore walls stained with microsphere aggregates were removed from the slices with perforating punches and saved in Eppendorf tubes. The rest of the soil slices were stored apart in a bottle. So, the microspheres retained in the contour of the macropores were quantified separately from the soil matrix as follows. The content of the tubes and bottles was weighed and suspended in 10 mL (pore walls) and 20 mL (matrix) of a non-ionic surfactant solution (Tween 20 in distilled water, 0.02%). Suspensions were shaken and homogenized for 10 s with an ultrasonic homogenizer. Aliquots (0.5 mL each, 3 replicates) were immediately pipetted and diluted in appropriate volumes of 0.02% Tween 20 and filtered through nitrocellulose membranes (pore size 0.45 µm, diam. 47 mm). Particle counting in the membranes was made using digital images obtained with a fluorescence laboratory magnifier and a digital camera. Bulk density ρ_b and the volumetric water content θ were determined at the end, after drying each slice at 105 ºC.

The average pore-water velocity v (Table 2) was calculated from the irrigation rate q and the average soil water content θ_{avg}:

$$v = q/\theta_{avg} \qquad \text{(eq. 4)}$$

The two-region physical non-equilibrium model was fitted to the experimental BTCs using the software STANMOD (CXTFIT Code). The optimal inverse solution was used to calculate the transport parameters. This model assumes that the soil porosity can be divided into two different regions: mobile and immobile [24]. The transport model is given by:

$$\theta_m \frac{\partial c_m}{\partial t} = \theta_m D \frac{\partial^2 c_m}{\partial x^2} - J_w \frac{\partial c_m}{\partial x} - \alpha(c_m - c_{im}) \qquad \text{(eq. 5)}$$

$$\theta_{im} \frac{\partial c_{im}}{\partial t} = \alpha(c_m - c_{im}) - \theta_{im} \mu_{im} c_{im} \qquad \text{(eq. 6)}$$

Where: θ is the volumetric water content [$L^3 L^{-3}$]; c is the concentration [ML^{-3}]; D is the dispersion coefficient [$L^2 T^{-1}$]; x and t are the distance [L] and time [T]; J_w is the volumetric water flux density [LT^{-1}]; α is the first-order kinetic coefficient between mobile and immobile zones [T^{-1}]; and μ is the first-order decay coefficient [T^{-1}]. The subscripts *m* and *im* indicate the mobile and immobile liquid regions. The dispersivity for the Br and MS (d and d_{MS}) was calculated by dividing the dispersion coefficient by the pore-water velocity.

We adjusted the following parameters: β, a dimensionless parameter for the partitioning in two-region transport model

$$\beta = \frac{\theta_m}{\theta} \qquad \text{(eq. 7)}$$

; ω, the dimensionless mass transfer coefficient

$$\omega = \frac{\alpha L}{\theta v} \qquad \text{(eq. 8)}$$

; and μ, the dimensionless first order decay coefficient for the immobile region

$$\mu = \frac{L\, \theta_{im}\, \mu_{im}}{\theta v}$$

(eq. 9)

The μ was adjusted only for the microspheres to model irreversible trapping in the immobile regions; μ was set to zero (no irreversible trapping) for the transport of Br^-.

The dimensionless 5%-arrival time of Br^- ($T_{5\%}$) was used to estimate the degree of preferential transport in the BTC. $T_{5\%}$ was calculated by considering the period of time (in pore volumes) it took for 5% of bromide to reach the bottom of column (see details in Koestel et al. (2013) [25]).

3 Results & Discussion

3.1 Soil structure differences from image analysis

The CT parameters were analyzed with the Shapiro-Wilk test in order to check that the data of each variable were normally distributed, and there was one exception: the branch length average (cm). Consequently, to examine the differences among the soil managements, we used a single factor ANOVA with all the variables but with the average branch length. With this one, the test employed was the Kruskal-Wallis. Through these tests, we observed and corroborated significant differences between the CT features of the plots studied (Table 3).

The CT-macropores in the ST plot presented the shortest averaged length branches and the most tortuous branches, while NT presented large and straight branches mostly generated by undisturbed decaying roots from the past crop. Bramorski et al. (2012)[26] proved that tortuosity increases a 56% after tillage, improving the water and sediment storage. The pores of the NT zone had, in general, the largest wall surface area, but they were not statistically different from the ST plot. The CT-macropores in the Org. plot and NT had similar average branch length and tortuosity, but the Org. A subzone had the largest CT-macropores because of the higher number of earthworm burrows. The lower values of the wall surface area in the two Org. zones, A and B, could be due to the type of pores: the walls of this pores were lined by earthworm cast, making the pores smooth and reducing their surface [27]. Root pores are responsible for the high circularity in the NT columns. The ST plot showed a slightly lower circularity than the organic plots, and that is because the Org. samples had, in some degree, earthworm pores, that are more circular than the pores produced by the shallow tillage, a feature already noted by Gantzer & Anderson [28]. Nevertheless, the organic plots (A and B) can not reach the level of circularity of the NT plot, and this can be explained by the type of vegetation: cultures have more circularity than grass and permanent vegetation [29,30]. It is important to note that the values showed in Table 3 are average values of all pores bigger than 0.24 mm, not only root or earthworm pores.

In the CT images, the tone of the pore walls of the plots with root and earthworm pores was slightly clearer than pore walls of the ST plot (HU values were as follows, Conv. ST, 136.4 ± 7.21; Conv. NT, 143.55 ± 3.69; Org. A, 142.65 ± 2.62; Org. B, 146.74 ± 6.2), but there were no significant differences between the plots. However, this increase in the density of the soil in the areas surrounding the earthworm burrows was already pointed by Rogasik et al. (2014) [31].

3.2 Solute and colloid transport and modeling

Pulses of a suspension of microspheres in KBr (500 mL, ≈ 2.5 pore volumes, PV) were applied in the NT and ST columns. For the Org. columns we used shorter pulses (350 mL ≈ 1.5 PV) to avoid the surface ponding observed in the first experiments. Mass balance of Br^- in the transport experiments indicates that 15 ± 5% was not eluted after 10 PV. This imbalance is commonly found in tracer experiments in structured soil, and is typically ascribed to solute transfer between mobile and immobile water regions of soil [32], and suggests physical retention of bromide in immobile zones. High organic matter content may also contribute to increasing retention [33]. The similarity in the mass balance between treatment plots indicates that the soil management had no influence on the unreactive transport. Poor relationships between soil macropore features and tracer transport were already reported for cracked paddy soils[34].

The transport models fitted fairly well for most of the Br^- in the columns ($R^2 > 0.95$, $P < 0.001$; between observed and predicted BTC data), as can be seen in Figure 2. The poorest fittings were obtained for three columns of the Org. plot considering the R^2: columns n# 10, 15 and 20, with R of 0.948, 0.943 and 0.946, respectively.

Table 2 summarizes the parameters of unreactive transport. The zones had similar transport parameters for Br^-, and only the solute dispersion coefficient (*D*) and the 5%-solute arrival time showed significant differences between zones.

The ST columns presented the largest *D*, 40.3 ± 22.8 $cm^2 h^{-1}$, but also had the largest deviations. Transport in ST may be influenced by the sharp density increase with depth and the associated pore network, namely a massive structure at the bottom crossed by few cracks. This pore network feature may expand the range of the pore water velocities, which can explain the large dispersion of Br^-. The NT also has a large *D*, 38.8 ± 6.2 cm^2h^{-1}, and this can be due to the large wall surface area of the pores, i.e., many root channels with different lengths and geometries that also increase the span of pore water velocities. On the other hand, organic soil columns had smaller mean *D* than the NT (Student *t*-test, $P < 0.05$); with 12.2 ± 6.8 cm^2h^{-1} for the Org. A, and 15.0 ± 10.1 cm^2h^{-1} for the Org. B.

The $T_{5\%}$ presented very small variation inside the groups. Values of this parameter were identical for the NT and ST soils, with 0.322 ± 0.001 PV and 0.325 ± 0.007 PV respectively. Means of this data showed significant differences between organic and conventional (*t*-test, $P < 0.001$). For the Org. A and Org. B the values were smaller 0.235 ± 0.003 and 0.207 ± 0.002 PV respectively (Figure 3). The values obtained are very similar to the ones reported by Koestel et al. (2012) [35], with a $T_{5\%}$ for the arable soils between 0.35 and 0.1. In this work, they also found a reduction of the $T_{5\%}$ in the arable soils with minimum tillage in the same way as in our work.

There is a good correlation between *D* and 5%-arrival time (Figure 4B) ($R = 0.545$, $P < 0.02$). That positive relation differs from the general negative relationship found by Koestel et al. (2012) [35]. However, there has to consider that the scale of our 5%-arrival time-dispersion parameter defines a small subset of the region shown in Koestel et al. (2012) [35]. Our data covers a rounded-shaped point cloud in the above reference that does not present a neat negative slope. The positive correlation may suggest that the larger the dispersion, the weaker preferential flow. Furthermore, these soils have a big amount of organic matter that has a strong influence over the dispersion and the 5%-solute arrival. Besides, the 5%-arrival is also related with the pore-water velocity ($R = 0.620$, $P < 0.02$), and has no significant correlation with the dispersivity ($R = 0.057$). These relationships indicate that the correlation between *D* and 5%-arrival time in our experiments can be spurious and the variation in the pore water velocity is the factor that determines the preferential flow.

The Smaller dispersion and the shorter $T_{5\%}$ in the organic plots can be explained by the bypass flow which in turn is favored by the earthworm pores. The effect of this type pores over the increasing of preferential flow, nutrient losses and tracer leachate was already demonstrated by many authors[36–38], and is responsible for the shorter time that the Br needed for traveling along the soil. The preferential flow can also explain the lower dispersion. However, in this case, we consider that the earthworm lining that covers the walls is the main factor. The lined walls seem to increase the pore water velocities and decrease their range of variation[27].

Inverse modeling of the microsphere BTCs (Figure 5) was carried out starting with the optimal set of parameters obtained for the Br dual porosity model. In this case, the addition of the coefficient of decay, μ, accounts for the irreversible retention of MS in the immobile zone. The BTCs of two columns (n# 10 and 19) presented a complex shape that could not be used to fit the model (Figure 5E). Transport parameters of MS were not different between zones, but the extreme values of the dispersion coefficient appear in the non-organic management: highest values were between 88 to 100 $cm^2\ h^{-1}$ in ST and the lowest 5 $cm^2\ h^{-1}$ in NT. The largest dispersion of MS in the ST was the same as in the Br case, suggesting that the underlying factors we conjectured for the large dispersion of Br can be valid for the MS. On the contrary, in the NT soil, straight root pores that contribute to a large dispersion of Br^- had not the same influence on the MS transport. And this happens even considering that these two zones have similar pore-water velocities.

3.3 Structure-transport relationships

When comparing the best fitting transport parameters and the data obtained from the X-ray CT images, we observed some significant correlations. For example, the dispersion coefficient for Br and the average pore surface were linearly correlated ($R = 0.803$, $P < 0.001$) (Figure 4C). In general, this trend is preserved for each zone. The non-organic soils had the pores with the largest wall surface area (217 ± 72 mm^2), and dispersion coefficient (39.5 ± 15.5 $cm^2\ h^{-1}$). Note the smaller averages for the organic field (133 ± 45 mm^2 and 13.6 ± 8.1 $cm^2\ h^{-1}$). The dispersion of Br is also correlated with the average number of slab voxels per branch (R = 0.728, P < 0.001), this means that the pores with larger branches presented a larger dispersion coefficient. On the other hand, the walls of the earthworm burrows in the organic field appear to be lined by a dense matrix. Lining tends to reduce the exchange of solute between mobile and immobile regions [39], that hinders the transport across the pore walls and decreases the spatial variation of distribution of transport velocities in the soil column. In consequence, in the plots with more earthworm pores we obtained smaller dispersion coefficients.

Best fitting model parameters can help to identify the dominant mechanisms of the transport of MS. We observed several good correlations between dual porosity model parameters and percentages of retention of MS and Br in the columns (Table 4). These correlations indicate that the model is consistent across most of the BTC experiments and soil management types. For example, the retention of microspheres is well described by the dimensionless MS transfer coefficient between matrix and macropores (ω_{MS}). Therefore, the high values of ω_{MS} the more particles may enter into the matrix in which a first order kinetic coefficient of particle removal, μ_{MS}, accounts for the trapping of the MS in the immobile region. Recall that the transport of Br^- was also well explained by the transfer between matrix and macropores. The significance of fitting the two-region model supports the hypothesis that the dual-porosity model describes the variability in the unsaturated transport of solutes and colloids reasonably well.

The $T_{5\%}$ in the overall columns is slightly correlated with the average pore surface area of the walls (is more a trend than a correlation since the significance is quite lower), suggesting a relation between preferential solute transport and the average pore surface (Figure 4A). That relation can be interpreted as the pores with larger wall surface area (i.e., more roughness and no lining) produce a physical retention in the transport of the Br. The greater preferential flow velocity in lined pores agrees with the well-known role of the earthworms in the fast transport along preferential pathways [40]. However, the relationship between $T_{5\%}$ and pore wall surface area in the ST columns is inverse to the rest of the zones (see Figure 4A). The reason for that inverse correlation is that the scale of arrival times in ST is compressed in a narrow interval (0.29 to 0.37 PV) and we cannot conclude with certainty anything with only four similar samples. However, if we discard these columns, the correlation is still valid.

The total end-point voxels and the size of the tails of the bromide BTC are also correlated (R = 0.54). End-point voxels represent dangling paths that end in the matrix; their presence could enhance solute transport between the mobile and immobile regions of the soil. The reversible mobile-immobile transfer is typically associated to solute tailing in the BTC. The interesting point here is that the macroscopic behavior of the dual-porosity transport is related to the description of the structure. The CT_{Matrix} shows a negative correlation with $T_{5\%}$ (R= - 0.56; $P < 0.02$), which indicates that the denser the matrix, the faster the Br^- transport across macropores. This relation suggests that a dense matrix difficult the solute transfer into immobile regions, channeling the solute flux through the macropores.

The data found by Safadoust et al. (2014)[41] support the results obtained in this section. The bromide transport parameters are related to the porosity: the larger the percentage of macropores the larger the dispersion and the mass exchange rate between the mobile and immobile zones.

The CT_{Matrix} of the entire column presents a negative correlation with the % of MS retained in the upper half, i.e., from 0 to 5 cm depth, with R = - 0.498; $P < 0.05$. There is a similar correlation (R = - 0.439, $P < 0.08$) between the CT_{Matrix} and the % of MS retained in the matrix regarding the total MS retention in the column (matrix and pore walls). We suggest that in columns with a lighter CT_{Matrix} MS enter easily into the matrix, where are retained, and, on the contrary, denser matrix favors the transport of the MS into macropores and decreases their capture into the matrix. Is noteworthy that this correlation becomes statistically significant (Figure 6) after discarding the column number 19 (R = - 0.643; $P < 0.02$). The column no. 19 of the Org. B plot presented huge macropores ending in the PVC ring (i.e., walls of the column) (Figure 1D); that configuration would enhance the transfer of MS into the matrix. Similarly, the correlation between the Br^- recovery and CT_{Matrix} increases after removing the column no. 19

(i.e., from R = 0.367 to R = 0.687; $P < 0.02$). We concluded that dead-end macropores and lighter matrix favor the retention of solute and colloids into the matrix.

4 Conclusion

The influence of soil management on the soil structure and on the solute and colloid transport properties was studied by analysis of CT images of intact soil columns, followed by breakthrough experiments of Br and microspheres. On the one hand, the CT characterization allowed us to find significant differences between the studied managements. On the other hand, the two-region physical non-equilibrium transport model fitted well the breakthrough of bromide and polystyrene latex microspheres. Organic management showed the highest preferential transport, which was related to the type of macropres: earthworm burrows with lined walls. The presence of lined walls and preferential transport were related with the small mass transfer coefficient between matrix and macropores in the dual-porosity model.

Indicators of the macropore network and matrix density obtained from CT and image analysis explained solute and colloid transport. Results showed a clear influence of the soil management on the morphological descriptors of the soil structure and transport properties. Correlations found in this work provide some experimental evidence of links between the geometry of the soil pore network and the transport.

5 Acknowledgments

Authors want to acknowledge their fund sources: D.S.G. are funded by Pre-doctoral Fellowship Program (FPU) of Spain's Ministry of Education FPU14/00681, and M.P. and P.P.R are funded by a post-doctoral fellowship awarded by Xunta de Galicia (POS-A/2013/171 *Plan I2C* and Gain program ED481B-2017/31, respectively). L.V.J. was additionally funded by CIA and BV1 research contracts (FEDER, *Xunta de Galicia*).

Authors thank the Centro de Desenvolvemento Agrogandeiro (Ourense) for allowing the sampling in their plots, and Oscar Lantes at the archaeometry unit RIADT-CACTUS services USC for the CT image acquisition with their dental 3D Cone-beam i-CAT scanner.

6 References

1. Coolman, R. M. & Hoyt, G. D. The Effects of Reduced Tillage on the Soil Environment. *Horttechnology* **3,** 143–145 (1993).

2. Hevia, G. G., Mendez, M. & Buschiazzo, D. E. Tillage affects soil aggregation parameters linked with wind erosion. *Geoderma* **140,** 90–96 (2007).

3. Rashidi, M. & Keshavarzpour, F. Effect of Different Tillage Methods on Grain Yield and Yield Components of Maize (Zea mays L.). *Int. J. Agric. Biol.* **9,** 274–277 (2007).

4. Cannell, R. Q. Reduced tillage in north-west Europe—A review. *Soil Tillage Res.* **5,** 129–177 (1985).

5. de Jonge, L. W., Kjaergaard, C. & Moldrup, P. Colloids and Colloid-Facilitated Transport of Contaminants in Soils. *Vadose Zo. J.* **3,** 321 (2004).

6. McDowell-Boyer, L. M. *et al.* Particle transport through porous media. *Water Resour. Res.* **22,** 1901–1921 (1986).

7. Soto-Gómez, D., Pérez-Rodríguez, P., López-Periago, J. E. & Paradelo, M. Sepia ink as a surrogate for colloid transport tests in porous media. *J. Contam. Hydrol.* **191,** 88–98 (2016).

8. Paradelo, M. *et al.* Effects of Past Copper Contamination and Soil Structure on Copper Leaching from Soil. *J. Environ. Qual.* **42,** 1852 (2013).

9. Kjaergaard, C., Poulsen, T. G., Moldrup, P. & de Jonge, L. W. Colloid Mobilization and

Transport in Undisturbed Soil Columns. I. Pore Structure Characterization and Tritium Transport. *Vadose Zo. J.* **3,** 413–423 (2004).

10. Katuwal, S., Arthur, E., Tuller, M., Moldrup, P. & de Jonge, L. W. Quantification of Soil Pore Network Complexity with X-ray Computed Tomography and Gas Transport Measurements. *Soil Sci. Soc. Am. J.* **79,** 1577 (2015).

11. Pires, L. F. *et al.* Soil structure changes induced by tillage systems. *Soil Tillage Res.* **165,** 66–79 (2017).

12. Lipiec, J. & Hatano, R. Quantification of compaction effects on soil physical properties and crop growth. *Geoderma* **116,** 107–136 (2003).

13. Perret, J. S., Al-Belushi, M. E. & Deadman, M. Non-destructive visualization and quantification of roots using computed tomography. *Soil Biol. Biochem.* **39,** 391–399 (2007).

14. Anderson, S. H., Heinze, D. J. & Peyton, R. L. Assessment of Selected Methods for Estimating Chemical Transport Parameters from Computed Tomographic Imaging. in *Procedia Computer Science* **61,** 460–465 (2015).

15. Anderson, S. H., Heinze, D. J. & Peyton, R. L. Computed Tomography-estimated Transport Velocity and Chemical Dispersivity in Undisturbed Geomedia. *Procedia Comput. Sci.* **36,** 643–648 (2014).

16. Luo, L., Lin, H. & Halleck, P. Quantifying Soil Structure and Preferential Flow in Intact Soil Using X-ray Computed Tomography. *Soil Sci. Soc. Am. J.* **72,** 1058 (2008).

17. Naveed, M. *et al.* Correlating Gas Transport Parameters and X-Ray Computed Tomography Measurements in Porous Media. *Soil Sci.* **178,** 60–68 (2013).

18. Schindelin, J. *et al.* Fiji: an open-source platform for biological-image analysis. *Nat. Methods* **9,** 676–682 (2012).

19. Sauvola, J. & Pietikäinen, M. Adaptive document image binarization. *Pattern Recognit.*

33, (2000).

20. Doube, M. *et al.* BoneJ: Free and extensible bone image analysis in ImageJ. *Bone* **47,** 1076–1079 (2010).

21. Wu, Y. S., van Vliet, L. J., Frijlink, H. W. & van der Voort Maarschalk, K. The determination of relative path length as a measure for tortuosity in compacts using image analysis. *Eur. J. Pharm. Sci.* **28,** 433–440 (2006).

22. Katuwal, S., Moldrup, P., Lamandé, M., Tuller, M. & De Jonge, L. W. L. W. Effects of CT Number Derived Matrix Density on Preferential Flow and Transport in a Macroporous Agricultural Soil. *Vadose Zo. J.* **14,** (2015).

23. van Staden, J. F., Mulaudzi, L. V & Stefan, R. I. On-line speciation of bromine and bromide using sequential injection analysis with spectrophotometric detection. *Anal. Bioanal. Chem.* **375,** 1074–1082 (2003).

24. Toride, N., Leij, F. J. & Van Genuchten, M. T. The CXTFIT code for estimating transport parameters from laboratory or field tracer experiments. *Res Rep* **Research R,** 1–138 (1995).

25. Koestel, J. K. *et al.* Links between soil properties and steady-state solute transport through cultivated topsoil at the field scale. *Water Resour. Res.* **49,** 790–807 (2013).

26. Bramorski, J., De Maria, I. C., e Silva, R. & Crestana, S. Relations Between Soil Surface Roughness, Tortuosity, Tillage Treatments, Rainfall Intensity and Soil and Water Losses From a Red Yellow Latosol. *Rev. Bras. Cienc. Do Solo* **36,** 1291–1297 (2012).

27. Pagenkemper, S. K. *et al.* The effect of earthworm activity on soil bioporosity – Investigated with X-ray computed tomography and endoscopy. *Soil Tillage Res.* **146,** 79–88 (2015).

28. Gantzer, C. J. & Anderson, S. H. Computed tomographic measurement of macroporosity in chisel-disk and no-tillage seedbeds. *Soil Tillage Res.* **64,** 101–111 (2002).

29. Rachman, A., Anderson, S. H. & Gantzer, C. J. Computed-Tomographic Measurement of Soil Macroporosity Parameters as Affected by Stiff-Stemmed Grass Hedges. *Soil Sci. Soc. Am. J.* **69,** 1609 (2005).

30. Udawatta, R. P., Anderson, S. H., Gantzer, C. J. & Garrett, H. E. Agroforestry and Grass Buffer Influence on Macropore Characteristics. *Soil Sci. Soc. Am. J.* **70,** 1763 (2006).

31. Rogasik, H., Schrader, S., Onasch, I., Kiesel, J. & Gerke, H. H. Micro-scale dry bulk density variation around earthworm (Lumbricus terrestris L.) burrows based on X-ray computed tomography. *Geoderma* **213,** 471–477 (2014).

32. van Genuchten, M. T. & Wierenga, P. J. Mass Transfer Studies in Sorbing Porous Media I. Analytical Solutions1. *Soil Sci. Soc. Am. J.* **40,** 473 (1976).

33. Larsbo, M., Koestel, J., Katterer, T. & Jarvis, N. Preferential Transport in Macropores is Reduced by Soil Organic Carbon. *Vadose Zo. J.* **15,** (2016).

34. Zhang, Z. B., Peng, X., Zhou, H., Lin, H. & Sun, H. Characterizing preferential flow in cracked paddy soils using computed tomography and breakthrough curve. *Soil Tillage Res.* **146,** 53–65 (2015).

35. Koestel, J. K., Moeys, J. & Jarvis, N. J. Meta-analysis of the effects of soil properties, site factors and experimental conditions on solute transport. *Hydrol. Earth Syst. Sci.* **16,** 1647–1665 (2012).

36. Edwards, W. M., Shipitalo, M. J., Owens, L. B. & Norton, L. D. Water and nitrate movement in earthworm burrows within long-term no-till cornfields. *J. Soil Water Conserv.* **44,** 240–243 (1989).

37. Shipitalo, M. J., Edwards, W. M. & Redmond, C. E. Comparison of water movement and quality in earthworm burrows and pan lysimeters. *J. Environ. Qual.* **23,** 1345–1351 (1994).

38. Shipitalo, M. J., Dick, W. A. & Edwards, W. M. Conservation tillage and macropore

factors that affect water movement and the fate of chemicals. *Soil Tillage Res*. **53,** 167–183 (2000).

39. Jarvis, N. J. A review of non-equilibrium water flow and solute transport in soil macropores: Principles, controlling factors and consequences for water quality. *European Journal of Soil Science* **58,** 523–546 (2007).

40. Kautz, T. *et al.* Nutrient acquisition from arable subsoils in temperate climates: A review. *Soil Biol. Biochem.* **57,** 1003–1022 (2013).

41. Safadoust, A. *et al.* Comparison of three models describing bromide transport affected by different soil structure types. *Arch. Agron. Soil Sci.* **62,** 674–687 (2015).

7 Figures

Figure 1. 3D representation of columns from each plot. A) ST (column number 6); B) NT (column number 7); C) Org. A (column number 8); and D) Org. B (column number 19).

Figure 2. Br modeling for one column of each zone. The two-region physical non-equilibrium model (dual porosity) was used.

Figure 3. $T_{5\%}$ (in pore volumes) results for the column averages of each zone. [a, b, c] Factors with same superscript in the key labels were not different (< 0.05) using a single factor ANOVA.

Figure 4. Relation between: A) the average pore surface and the $T_{5\%}$ (in pore volumes); B) the dispersion of Br and the $T_{5\%}$ (in pore volumes); and C) the average pore surface and the dispersion of Br.

Figure 5. Microsphere modelling for: A), B), C) and D) One column of each zone; and E) Two columns that we could not model: nº 10 (Org. A) and nº 19 (Org. B). C/C_0 is the relative concentration.

Figure 6. Relation between the % of particles retained in the matrix and the CT_{Matrix}.

A) ST, Nº 6

B) NT, Nº 7

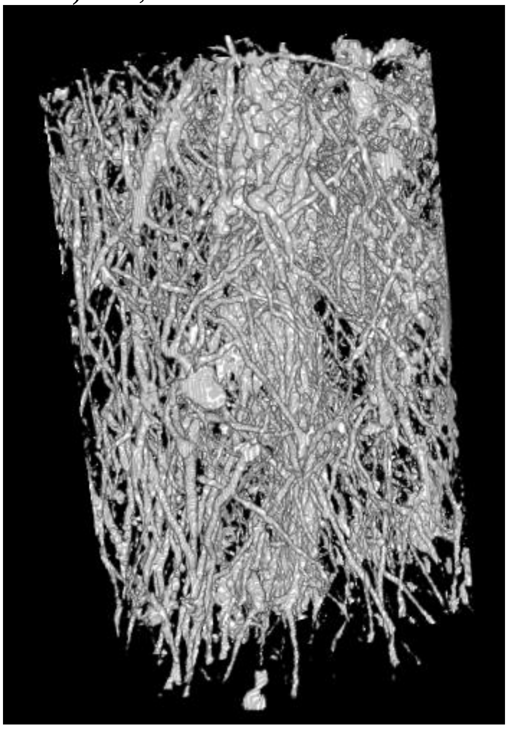

C) Org. A, Nº 8

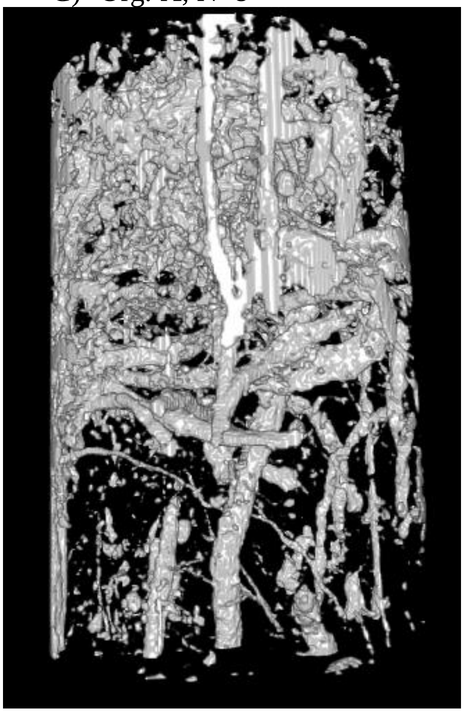

D) Org. B, Nº 19

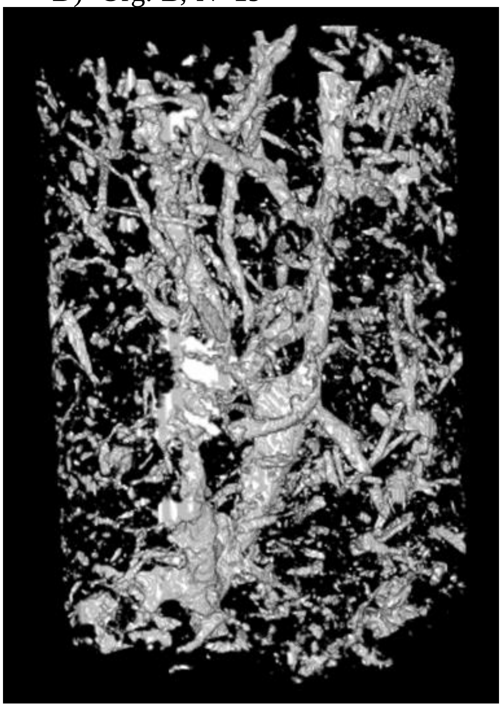

Figure 1.

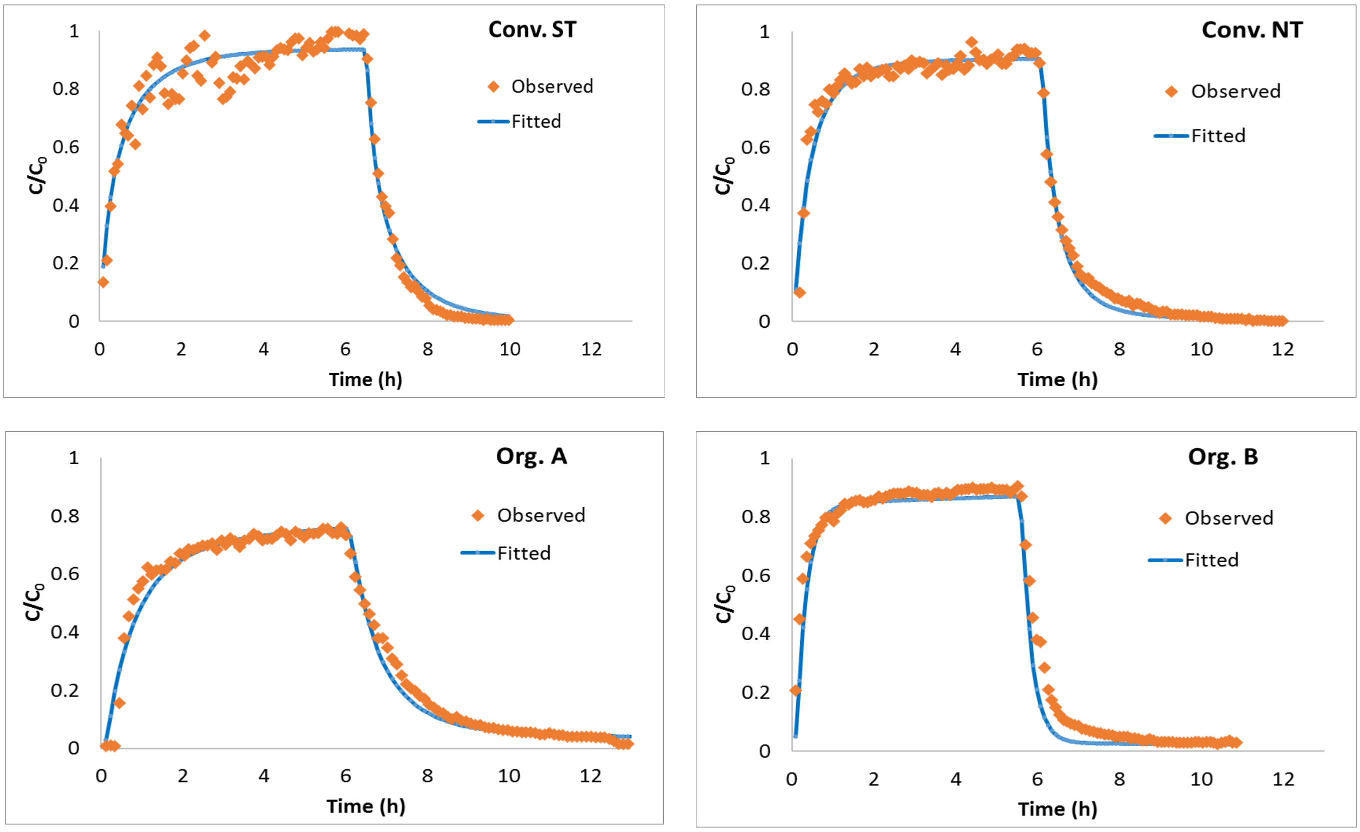
Conv. ST
Conv. NT
Org. A
Org. B
Observed
Fitted
c/c$_0$
Time (h)
0
0.2
0.4
0.6
0.8
1
0
2
4
6
8
10
12

Figure 2.

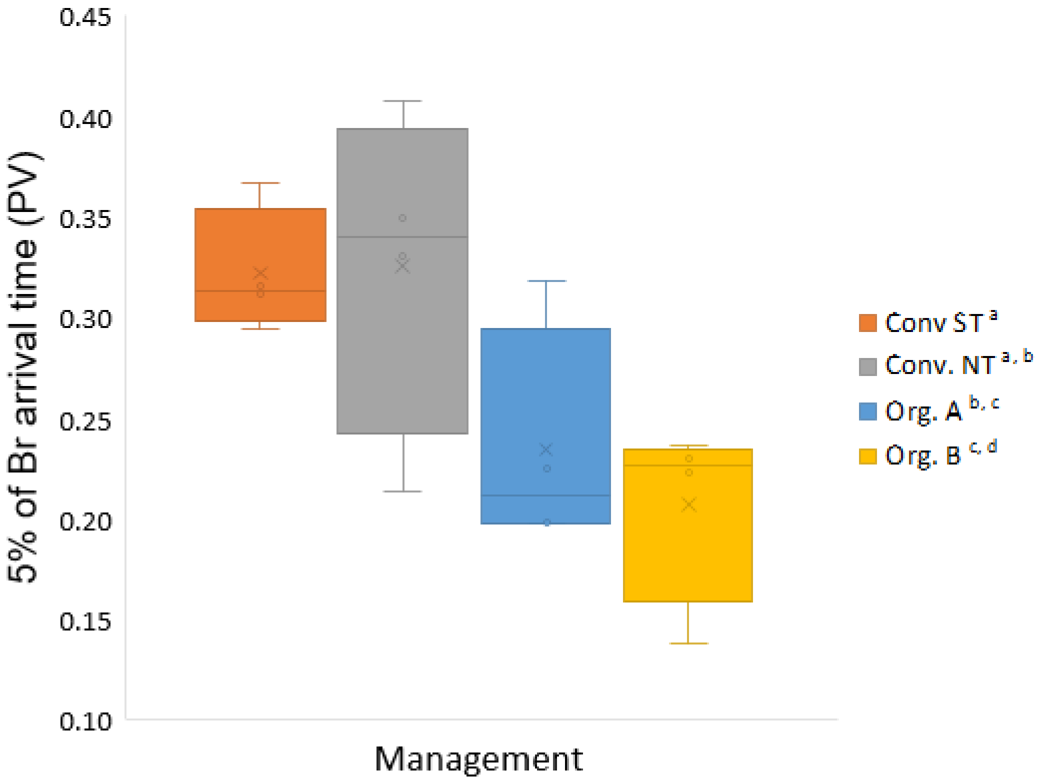
0.45
0.40
0.35
0.30
0.25
0.20
0.15
0.10
5% of Br arrival time (PV)
Management
Conv ST a
Conv. NT a, b
Org. A b, c
Org. B c, d

Figure 3.

A)

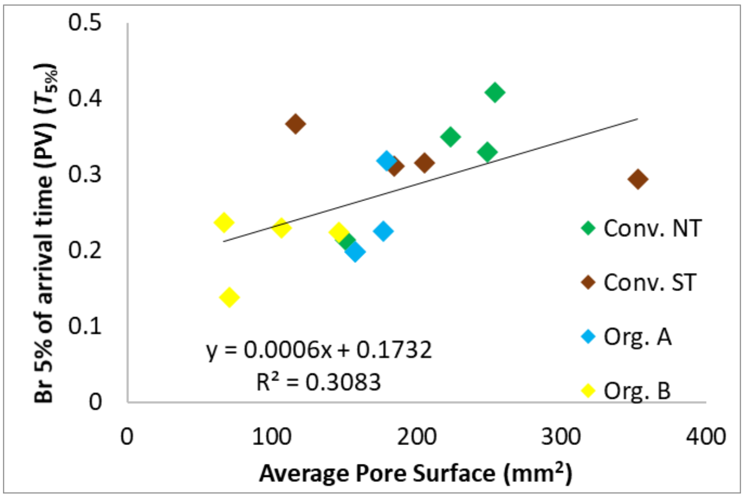
Br 5% of arrival time (PV) ($T_{5\%}$)
0.5
0.4
0.3
0.2
0.1
0
0
100
200
300
400
Average Pore Surface (mm²)
Conv. NT
Conv. ST
Org. A
Org. B
y = 0.0006x + 0.1732
R² = 0.3083

B)

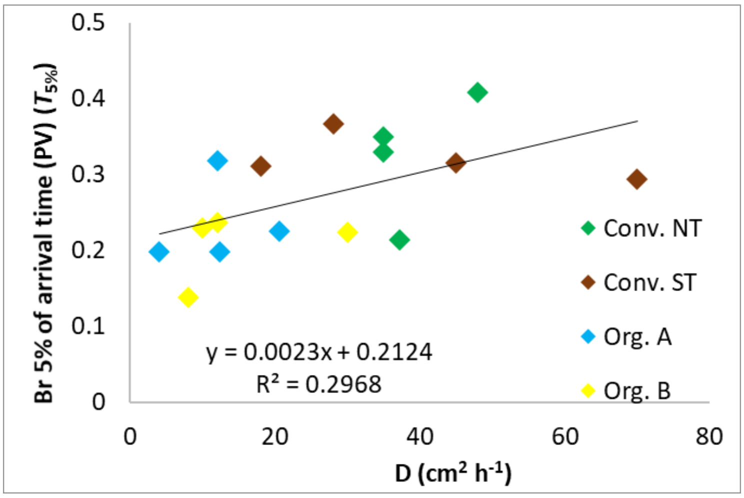
Br 5% of arrival time (PV) ($T_{5\%}$)
0.5
0.4
0.3
0.2
0.1
0
0
20
40
60
80
D (cm² h⁻¹)
Conv. NT
Conv. ST
Org. A
Org. B
y = 0.0023x + 0.2124
R² = 0.2968

C)

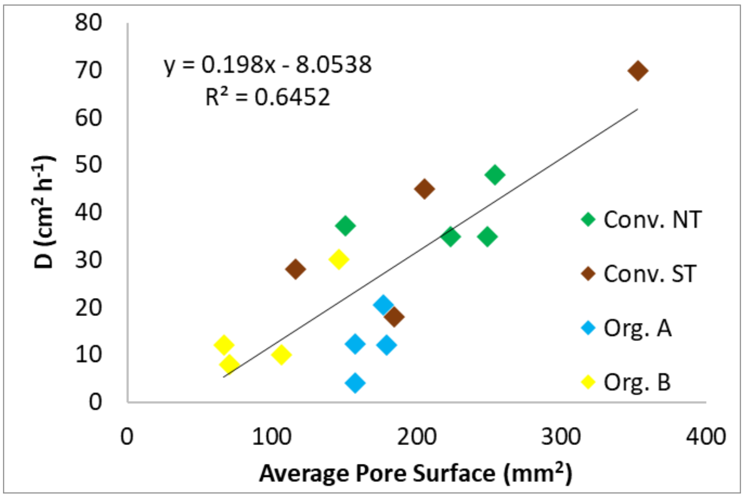
D (cm² h⁻¹)
80
70
60
50
40
30
20
10
0
0
100
200
300
400
Average Pore Surface (mm²)
y = 0.198x - 8.0538
R² = 0.6452
Conv. NT
Conv. ST
Org. A
Org. B

Figure 4.

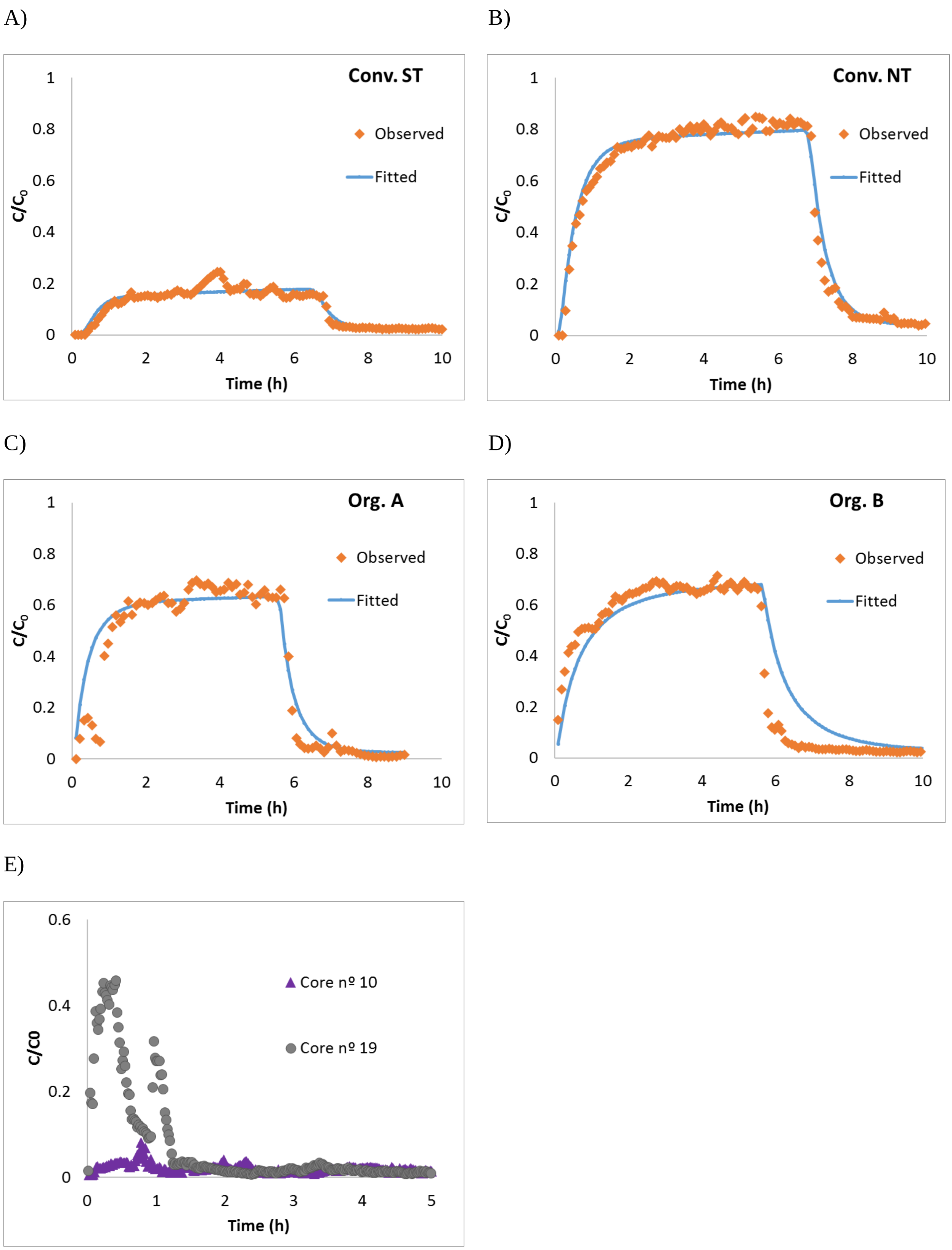
A)
Conv. ST
Observed
Fitted
c/C0
1
0.8
0.6
0.4
0.2
0
0
2
4
6
8
10
Time (h)
B)
Conv. NT
Observed
Fitted
c/C0
1
0.8
0.6
0.4
0.2
0
0
2
4
6
8
10
Time (h)
C)
Org. A
Observed
Fitted
c/C0
1
0.8
0.6
0.4
0.2
0
0
2
4
6
8
10
Time (h)
D)
Org. B
Observed
Fitted
c/C0
1
0.8
0.6
0.4
0.2
0
0
2
4
6
8
10
Time (h)
E)
Core nº 10
Core nº 19
c/C0
0.6
0.4
0.2
0
0
1
2
3
4
5
Time (h)

Figure 5.

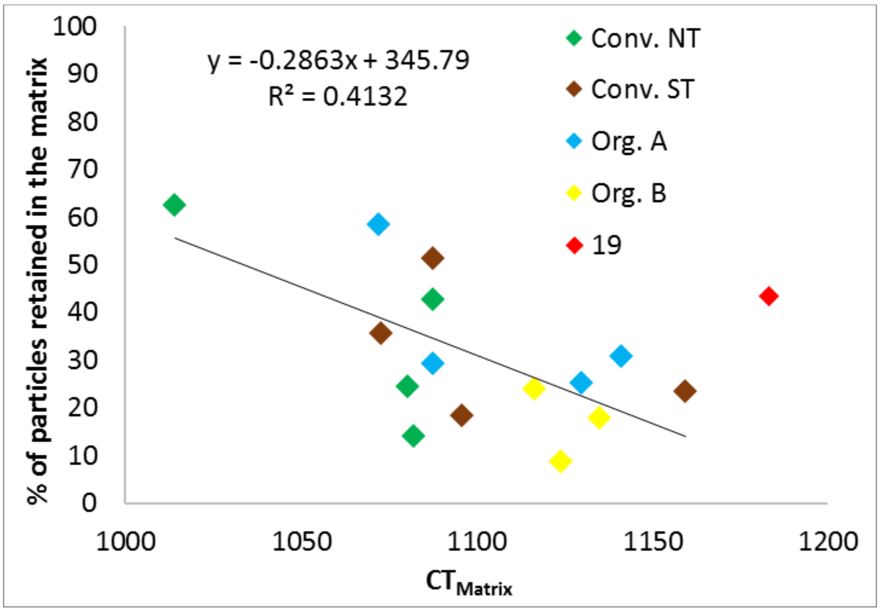
y = -0.2863x + 345.79
R² = 0.4132
Conv. NT
Conv. ST
Org. A
Org. B
19
% of particles retained in the matrix
0
10
20
30
40
50
60
70
80
90
100
1000
1050
1100
1150
1200
CT Matrix

Figure 6.

8 Tables

Table 1. Soil texture results for the three plots with standard deviations.

Management	*% Coarse Sand (> 0.5mm)*	*% Fine Sand (0.5 – 0.05 mm)*	*% Silt (0.05 – 0.002mm)*	*% Clay (< 0.002mm)*	*% Organic Matter*
Conv. NT (n =4)	*46.2 ± 0.5*	*26.1 ± 0.9*	*5.7 ± 2.9*	*10.9 ± 1.2*	*11.1 ± 2.6*
Conv. ST (n =4)	*42.9 ± 2.4*	*28.3 ± 1.7*	*5.3 ± 4.1*	*11 ± 0.6*	*12.5 ± 4.6*
Org. (n =8)	*44.5 ± 0.2*	*29 ± 0.4*	*8.1 ± 0.3*	*9.2 ± 0.7*	*8.5 ± 0.5*

Table 2. Parameters of the moisture of each column and obtained from the Br^- modelling.

Zone	*Column number*	*v (cm h⁻¹)*	θ_s	θ	*D (cm² h⁻¹)*	*d (cm)*	β	ω
Conv. ST	6	2.71	0.51	0.47	45	16.62	0.15	0.180
	12	3.48	0.43	0.40	28	8.05	0.09	0.270
	14	2.60	0.49	0.44	70	26.94	0.05	0.019
	16	2.67	0.43	0.37	18	6.75	0.23	0.150
Average		2.86 ± 0.41	0.46 ± 0.04	0.42 ± 0.04	40.25 ± 22.75	14.59 ± 9.32	0.13 ± 0.08	0.15 ± 0.10
Conv. NT	2	3.41	0.41	0.4	37.2	10.91	0.10	0.056
	4	2.67	0.45	0.4	35	13.11	0.05	0.083
	5	2.51	0.42	0.4	35	13.94	0.08	0.077
	7	2.6	0.47	0.45	48	18.46	0.19	0.170
Average		2.80 ± 0.41	0.44 ± 0.03	0.41 ± 0.03	38.80 ± 6.22	14.11 ± 3.17	0.11 ± 0.06	0.10 ± 0.05
Org. A	3	2.01	0.50	0.47	20.55	10.20	0.14	0.191
	8	2.81	0.47	0.43	12	4.26	0.15	0.130
	9	0.36	0.51	0.47	12.3	34.39	0.02	0.004
	10	0.36	0.57	0.52	4	11.2	0.05	0.300
Average		1.39 ± 1.23	0.51 ± 0.04	0.47 ± 0.04	12.21 ± 6.76	15.01 ± 13.27	0.09 ± 0.06	0.16 ± 0.12
Org. B	13	2.83	0.48	0.46	10	3.54	0.08	0.130
	15	1.27	0.50	0.48	30	23.59	0.10	0.100
	19	0.73	0.47	0.44	8	10.89	0.06	0.001
	20	3.03	0.45	0.42	12	3.96	0.15	0.100
Average		1.97 ± 1.14	0.47 ± 0.02	0.45 ± 0.03	15.00 ± 10.13	10.49 ± 9.36	0.10 ± 0.04	0.08 ± 0.06

v [$L\ T^{-1}$] is the pore water velocity; θ_s is the saturated water content; θ is the volumetric water content after saturation and a drainage of 1 hour; *D* is the dispersion coefficient for the bromide [$L^2\ T^{-1}$]; *d* is the dispersivity [L]; β, is a dimensionless parameter for the partitioning of bromide in two-region transport model; and ω is the dimensionless mass transfer coefficient of bromide.

Table 3. CT macroporosity descriptors (with standard deviation) influenced by management type, after a single factor ANOVA or a Kruskal-Wallis test (for the Average Branch length).

	Conv. ST	*Conv. NT*	*Org. A*	*Org. B*
CT Macroporosity (%)	7.56 ± 3.38^{ab}	4.65 ± 1.4^{b}	9.52 ± 2.55^{a}	4.34 ± 2.36^{b}
Total Volume (cm^3)	39.71 ± 13.98 ^{ab}	26.57 ± 8.98 ^{b}	55.73 ± 11.71^{a}	25.62 ± 15.67^{b}
Average Pore Surface (cm^2)	2.15 ± 1.00^{ab}	2.19 ± 0.48^{a}	1.68 ± 0.12^{a}	0.98 ± 0.37^{b}
Total Slab Voxels	65669 ± 18217^{ab}	89604 ± 13468^{b}	88333 ± 23452^{a}	45467 ± 25580^{b}
Total Branch Length (m)	20.7 ± 5.99^{ab}	26.35 ± 4.1^{a}	27.52 ± 7.53^{a}	13.95 ± 8.13^{b}
Average Branch Length (cm)	0.29 ± 0.009^{a}	0.45 ± 0.063^{b}	0.3 ± 0.022^{a}	0.3 ± 0.019^{a}
Circularity	0.51 ± 0.015^{a}	0.65 ± 0.045^{b}	0.55 ± 0.027^{a}	0.62 ± 0.019^{b}
Average Tortuosity	1.291 ± 0.008^{b}	1.252 ± 0.017^{a}	1.287 ± 0.009^{ab}	1.279 ± 0.013^{ab}
Average Tortuosity (pores larger than 10 mm)	1.48 ± 0.16^{b}	1.24 ± 0.061^{a}	1.65 ± 0.24^{b}	1.37 ± 0.09^{ab}

$^{a,\,b}$ different superscript showed significant differences between groups with different management at a probability value $P < 0.05$.

Table 4. Pearson's R coefficient for the correlation between some parameters of microsphere modeling and the retention.

	D_{MS} (cm^2 h^{-1})	β_{MS}	ω_{MS}	μ_{MS}
% MS Recovered	0.054	-0.553*	-0.673**	-0.796**
% MS Retained	-0.488	0.505	0.797**	0.803[a]
Up_Retention (Retention in the upper half of the column)	-0.470	0.514	0.816**	0.839[a]
Matrix_Retention	-0.410	0.637*	0.832*	0.847[a]
Pore_Retention	-0.560*	-0.535	-0.073	-0.093
Br (%)	0.290	-0.540*	-0.628*	-

[a] High correlation results of the leverage influence from one single observation.

D_{MS} is the dispersion coefficient for the MS [L]; β_{MS}, is a dimensionless parameter for the partitioning of MS in two-region transport model; ω_{MS} is the dimensionless mass transfer coefficient of MS; and μ_{Ms} is the first-order decay coefficient [T^{-1}] for the MS.